ARTICLE IN PRESS

Deep-Sea Research I xxx (xxxx) xxx

FISEVIER

Contents lists available at ScienceDirect

Deep-Sea Research Part I

journal homepage: http://www.elsevier.com/locate/dsri



Abundance of low-temperature axial venting at the equatorial East Pacific Rise

Sheng Chen a,b,*, Chunhui Tao c,d,**, Christopher R. German b

- a Ocean Technology and Equipment Research Center, School of Mechanical Engineering, Hangzhou Dianzi University, Hangzhou, 310018, China
- ^b Department of Geology and Geophysics, Woods Hole Oceanographic Institution, Woods Hole, MA, 02543, USA
- ^c Key Laboratory of Submarine Geosciences, SOA & Second Institute of Oceanography, MNR, Hangzhou, 310012, China
- ^d School of Oceanography, Shanghai Jiao Tong University, Shanghai, 200240, China

ARTICLE INFO

Keywords: Hydrothermal venting Low temperature flow East pacific ridge ORP

ABSTRACT

Since their first discovery, predictions of the incidence of high temperature submarine vents has been made from along-axis surveys for the presence or absence of particle-rich "black smoker" hydrothermal plumes in the overlying water column. Recent work along intermediate and fast spreading ridges, however, has shown that abundant lower-temperature forms of seafloor fluid flow might be overlooked by this approach. Here, we report new data that allow us to test for both high- and low-temperature venting along the fast-spreading (110-132 mm/yr) equatorial East Pacific Rise (EPR), between 1.9°N and 4.9°S. We identify at least 32 discrete sites of hydrothermal activity, of which just 11 would have been resolved by particle-plume only survey methods. Such an approach would lead to a predicted frequency of high-temperature venting (Fs) along this section of the EPR of 4.2 sites/100 km, consistent with other particle-plume only surveys conducted under the auspices of InterRidge. When we include ORP sensor data to prospect for near-seafloor evidence of low-temperature venting, however, the calculated spatial frequency (Fs) for all styles of seafloor fluid flow increases by more than 3-fold, to Fs \geq 15.5 sites/100 km. Hence, this study provides confirmation that low-temperature venting should be widespread along all fast-spreading mid-ocean ridges. While an appreciation of the importance of low-temperature axial venting to geophysical fluxes (heat, mass) is well established, our results reveal evidence for low-temperature fluid flow that is out of geochemical (redox) equilibrium with the overlying water column. Consequently, these fluxes may also play an important but previously overlooked role in global-scale ocean biogeochemical cycles.

1. Introduction

Following the first discovery of submarine hydrothermal activity in the late 1970s (Corliss et al., 1979; Spiess et al., 1980) it was soon demonstrated that the presence of high-temperature seafloor venting could be inferred from dispersing non-buoyant plume signatures in the overlying water column (e.g. Klinkhammer et al., 1985; 1986; Nelsen et al., 1987). Subsequently, the development of Miniature Autonomous Plume Recorders (MAPRs: Baker and Milburn, 1997) allowed the international InterRidge community to demonstrate that submarine venting is present in all ocean basins and along ridges of all spreading rates (Baker and German, 2004; Beaulieu et al., 2013, 2015).

Recently, however, Baker et al. (2016) have shown that such

particle-plume only approach may have overlooked an abundance of low-temperature hydrothermal flow. New Oxidation-Reduction Potential (ORP) sensor data, collected along intermediate to fast-spreading ridges (50-100 mm/yr), suggest that the true incidence of seafloor venting may be a factor of 3-6 times higher than would be predicted from optical back-scatter anomalies alone. Here, we extend that approach to investigate the abundance of low and high temperature venting along an even faster-spreading section of ridge-crest. The East Pacific Rise (EPR) between 1.9°N and 4.9°S (Fig. 1), total ~758 km, comprises four first-order segments, separated by transform faults, with spreading rates that increase, north to south, from ~110 mm/yr to 132 mm/yr (DeMets et al., 1990). Fieldwork for this study was stimulated by initial indications of hydrothermal activity

https://doi.org/10.1016/j.dsr.2020.103426

Received 14 June 2020; Received in revised form 23 October 2020; Accepted 23 October 2020 Available online 7 November 2020 0967-0637/© 2020 Elsevier Ltd. All rights reserved.

^{*} Corresponding author. Ocean Technology and Equipment Research Center, School of Mechanical Engineering, Hangzhou Dianzi University, Hangzhou, 310018. China.

^{**} Corresponding author. Key Laboratory of Submarine Geosciences, SOA & Second Institute of Oceanography, MNR, Hangzhou, 310012, China. *E-mail addresses*: chensh@hdu.edu.cn (S. Chen), taochunhuimail@163.com (C. Tao).

within this study area detected during Chinese DY115-17 cruise. Prior to this study, the only evidence for venting in this entire region came from a report of photographic evidence for a "biologically active" site near 1.73°N (Shank et al., 2000).

2. Methods

A series of cruises sponsored by China Ocean Mineral Resources R&D Association (COMRA) systematically surveyed for seafloor hydrothermal activity along the EPR 1.9°N to 4.9°S between 2008 and 2011. Following initial detection of possible hydrothermal signals during Cruise DY115-17 (Tao et al., 2008), a series of follow-on cruises were conducted during which a series of deep-tow surveys were conducted both for seafloor imaging (to be described elsewhere) and water column plume surveys (the focus of this study). A detailed description of our methodology, including both at-sea instrument deployments and post-cruise data reduction, is provided in an accompanying Data Brief (Chen et al., 2020). In summary, multiple (2–6) MAPR instruments (Baker and Milburn, 1997) were attached to a deep-tow cable and deployed at known heights, between 20 and 450 m above a deep-tow package that was equipped with video, still cameras and an in situ Oxidation-Reduction Probe (ORP) sensor. This deep-tow package was towed at ~5 m above the seafloor using real-time video to guide lowering and raising of the package to maintain altitude (Fig. 2),

although micro-topographical variability did occasionally cause contact with the seafloor. The track lines for this study are shown in Fig. 1 with color coding (red, black) to indicate which of the surveys did or did not reveal evidence of seafloor fluid flow, respectively. A full list of all survey lines completed, including the USBL (ultra-short baseline navigated) start and end points of each near-seafloor survey is published in an accompanying data-brief (Chen et al., 2020). Topographic data presented in this study are reproduced from multibeam bathymetric surveys conducted independently using a Simrad EM120 multibeam aboard R/V Dayang Yihao cruises to the same area (Tao et al., 2008).

In this paper, we focus exclusively on those deep-tow surveys where significant in situ hydrothermal anomalies were detected (red track-lines in Fig. 1). For optical back-scatter anomalies, we have followed the data-reduction protocols of Walker et al. (2004) and Baker et al. (2014, 2016) to calculate turbidity anomalies (Δ NTU) and then, to be conservative, we have restricted ourselves to only discussing plumes where Δ NTU \geq 0.005. Similarly, we have followed the same approach as Baker et al. (2016) for the treatment of ORP sensor data and conservatively defined a statistically significant ORP anomaly as one that exhibits a rapid overall decrease of \geq 5 mV before beginning recovery toward its pre-anomaly voltage.

Combining our two sensor types, we find that we can variously combine Δ NTU and ORP anomalies to infer four different categories of seafloor fluid flow as defined below.

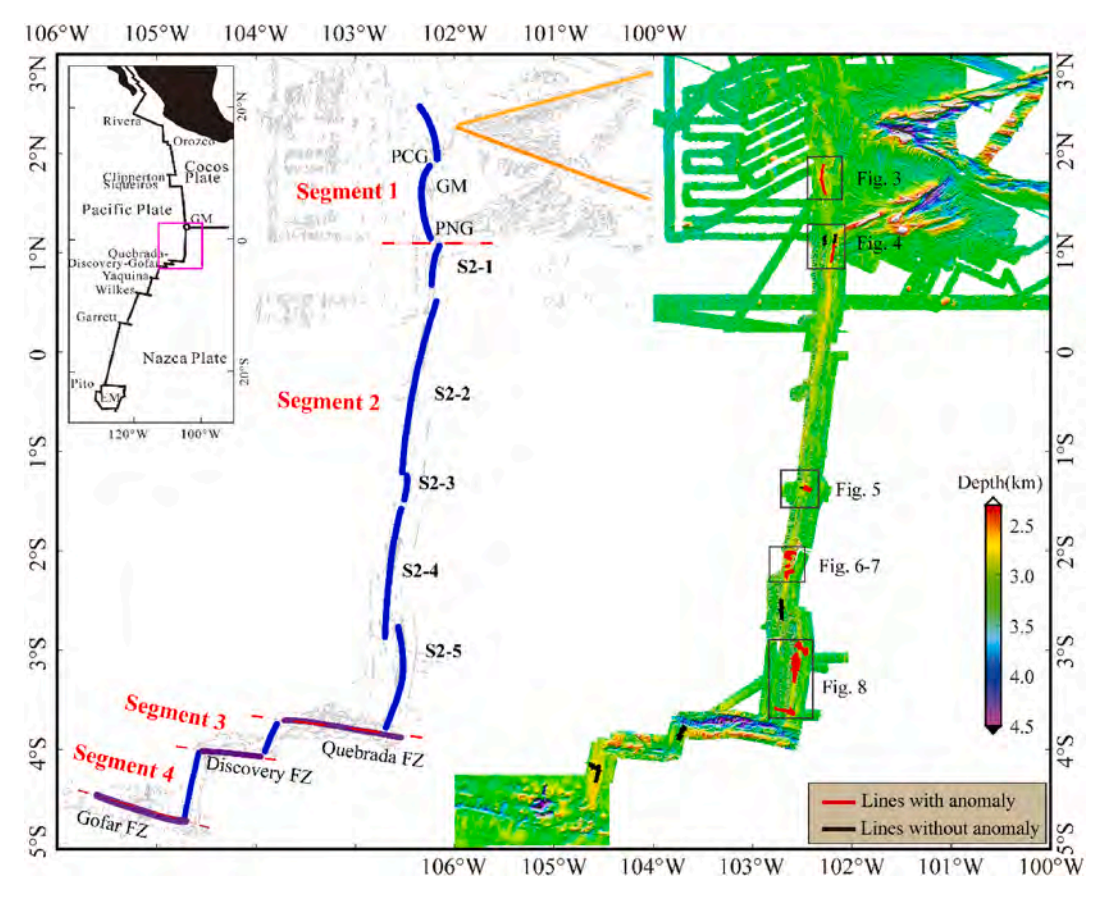


Fig. 1. Overview of the study area. *Inset*: location of the study area (magenta box) in the East Pacific, spanning plate boundaries between the Pacific Plate and, from north to south, the Cocos plate, the Galapagos Microplate (GM) and the Nazca Plate (EM = Easter Microplate). *Main Figure*: Schematic interpretation (left) and multibeam survey data (right) of the ridge segmentation determined during the 2008–2011 surveys of the EPR. Blue lines (at left) demarcate a series of first- and second-order axial ridge segments, and yellow lines (at left) represent the boundary of Galapagos spreading center. Segment 1 extends from the Pacific-Cocos-Galapagos triple junction (PCG) in the north to the Pacific-Nazca-Galapagos triple junction (PNG), while further south, segments 2, 3 & 4 are offset from one another by three major transform faults (Quebrada, Discovery and Gofar fracture zones). Segment 2 is further subdivided into five second-order ridge segments separated by overlapping spreading centers identified from the ridge-crest bathymetry (right hand panel) at 0.7°N, 1.2°S, 1.5°S and 2.8°S (Lonsdale, 1989). Colored lines superimposed on the multibeam bathymetry (at right) show track lines for the water column surveys reported on in this study that either did (red) or did not (black) reveal evidence for fluid flow at the underlying seafloor. (For interpretation of the references to color in this figure legend, the reader is referred to the Web version of this article.)

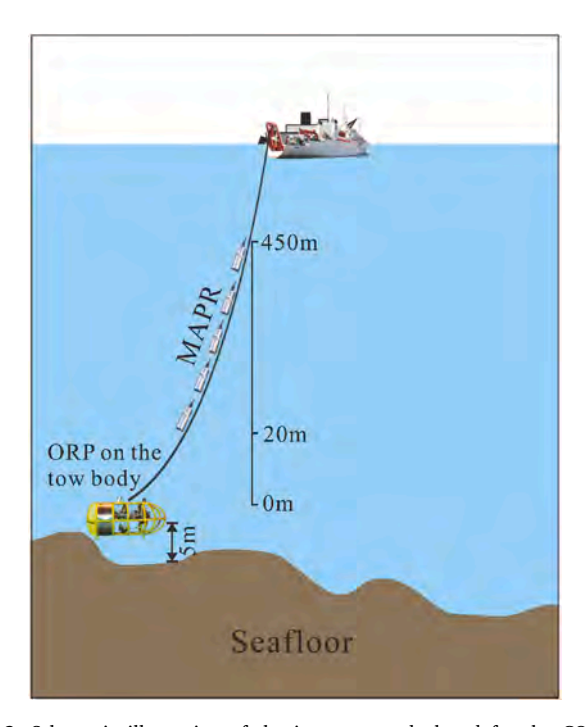


Fig. 2. Schematic illustration of the instruments deployed for the COMRA (2008–2011) EPR 1.9° N- 4.9° S surveys. Open cage represents the deep-tow package deployed at \sim 5 m above the seabed and equipped with an *in situ* ORP sensor. Grey rectangles represent a series of MAPRs (equipped with optical back-scatter sensors) mounted on the same deep-tow cable at known distances (20–450 m) above the tow body. The schematic is representative, not intended to show specifically the number or location of MAPRs for every tow. The actual number and location are specified for each tow shown in Figs. 3–8.

- (1) High T: Wherever lenses of NTU anomalies are detected in midwater (typically ≥100 m above the seafloor) they can be inferred to reflect the presence of high-temperature "black smoker" plumes. Such ΔNTU signals may or may not be accompanied by in situ ORP anomalies at the underlying seafloor, depending on whether the towed package was close to, or far from any underlying vent-source (German et al., 2008).
- (2) Low T: Wherever near-seabed ORP anomalies are observed, without accompanying NTU anomalies, a local source of lowtemperature hydrothermal flow is inferred.
- (3) Undifferentiated: Wherever near-seabed ORP anomalies are observed, co-located with optical backscatter anomalies, some form of seafloor fluid flow can be inferred to be present but whether such signals arise due to high-T or lower-T flow cannot be differentiated.
- (4) Suspected: When only near-seabed NTU anomalies are detected, in the absence of ORP anomalies, we can only suspect that seafloor fluid flow may be present. To be conservative, such suspected sites are not included in our calculations of vent-site distributions/ frequency along axis.

3. Results

In total, we conducted a cumulative length of $\sim\!305$ km of deep-tow surveys between $1.9^{\circ}N$ and $4.9^{\circ}S$, EPR (Fig. 1). The full data set is documented in an accompanying report submitted in conjunction with this manuscript (Chen et al., 2020) which also documents the data reduction processes used to analyze those data. Here, we focus upon the results from that subset of our survey lines where significant hydrothermal plume anomalies were detected (Fig. 1). Plots of these data are presented in Figs. 3–9 and an overview of the key results are summarized in Table 1. Letters A-Z refer to areas discussed in the text in the order in which they arise, from North to South. When more than one

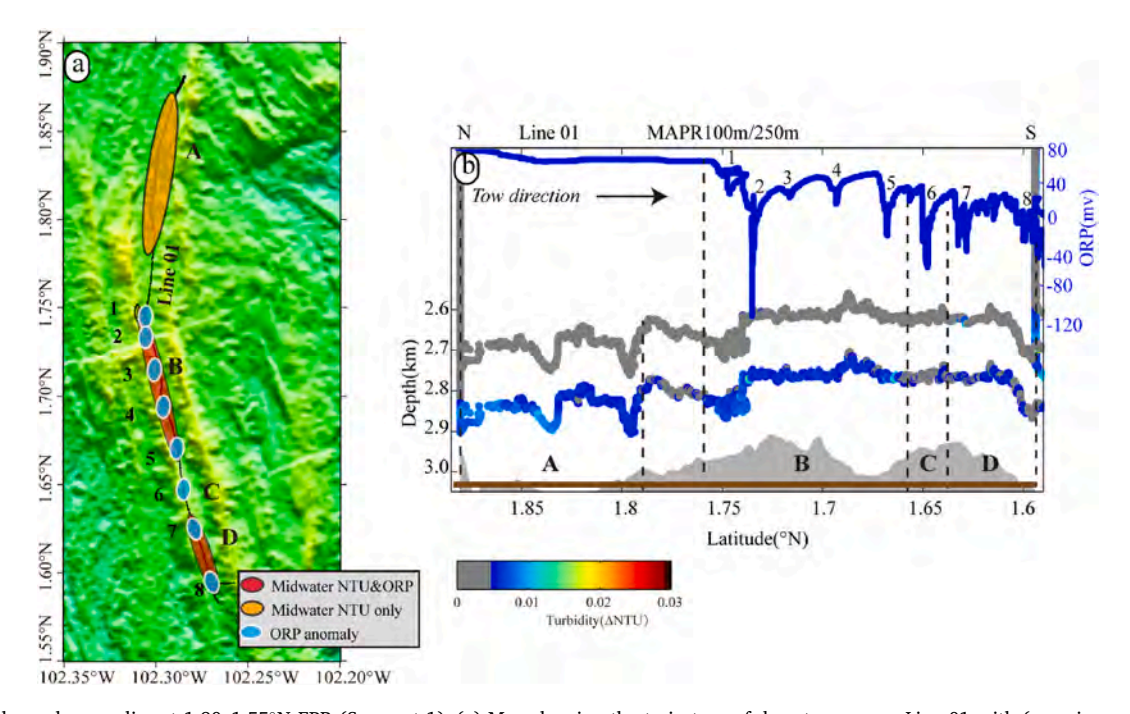


Fig. 3. Hydrothermal anomalies at 1.90–1.55°N EPR (Segment 1). (a) Map showing the trajectory of deep-tow survey Line 01 with (superimposed) color coded ellipses: pale blue = locations of near-bottom ORP anomalies; red = mid-water NTU anomalies overlying seafloor ORP anomalies; orange = mid-water NTU anomalies with no underlying ORP anomalies. (b) Vertical along-axis plot of near-bottom ORP data (upper trace) and MAPR NTU (turbidity) anomalies from the same deep-tow survey Line 01. Values for ORP are presented on the right-hand axis and MAPR depths are at left. See label at top axis for deployment heights of MAPRs above deep-tow package and color bar below bottom axis for △NTU. The gray-shaded area represented bathymetry profile under the deep-tow trackline and it was mapped by the ship during the deep-tow. The dashed lines are the boundaries of each area which was accompanied by NTU anomalies or ORP anomalies, or both. Letters A-D and numbers 1–8 refer to hydrothermal anomalies discussed in the text and Table 1. (For interpretation of the references to color in this figure legend, the reader is referred to the Web version of this article.)

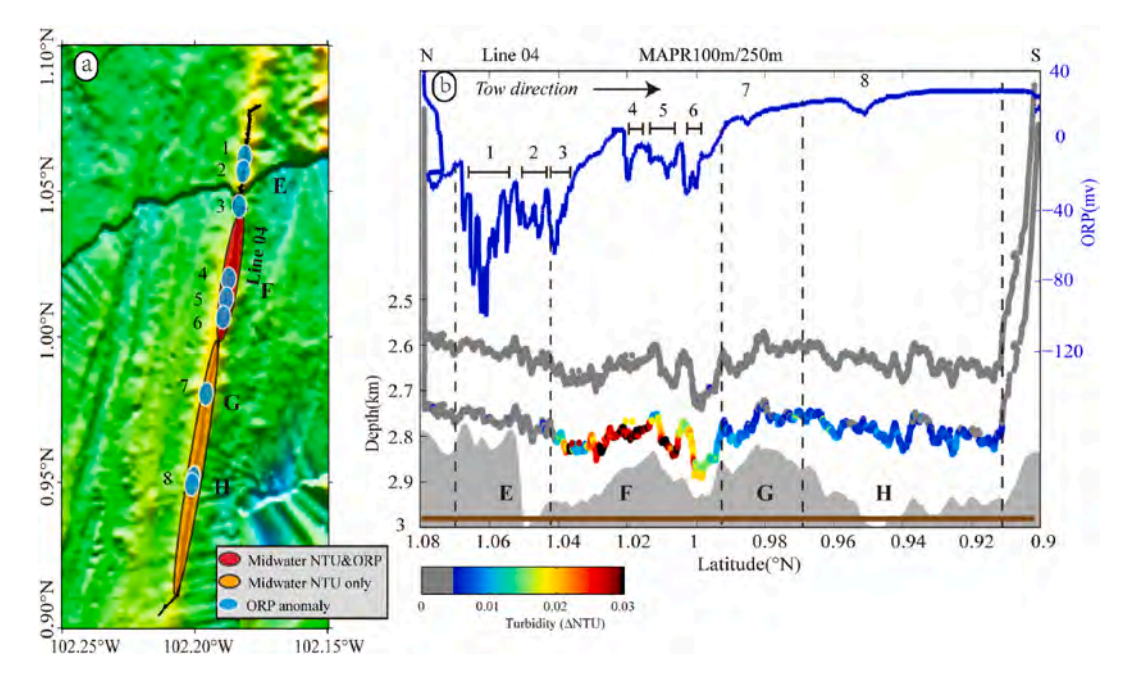


Fig. 4. Hydrothermal anomalies at 1.10–0.90°N EPR (Segment 2–1). (a) Map showing the trajectory of deep-tow survey Line 04 with (superimposed) ellipses with the same color coding as for Fig. 3a. (b) Vertical along-axis plot of ORP data and △NTU from the same deep-tow survey Line 04. See Fig. 3b for other plot details. Letters E-H and numbers 1–8 refer to hydrothermal anomalies discussed in the text. (For interpretation of the references to color in this figure legend, the reader is referred to the Web version of this article.)

hydrothermal site has been inferred within one study-area, sites are further annotated using Arabic numerals.

In segment 1, at least nine different sets of hydrothermal anomalies were detected across four separate areas (labelled A-D in Fig. 3). In our analysis (see previous section and an accompanying Data Brief (Chen et al., 2020)), these reveal a minimum of at least three separate High T vent sources (A, B, D) and at least one site of Low T flow (Fig. 3, #6). Because multiple near-seafloor ORP anomalies that coincide with above-bottom NTU anomalies are interpreted as originating from a minimum of 5 separate sources in Area B and two in Area D, our analysis requires that *at least* 5 further sources must be present (4 in Area B, 1 in Area D) and we can only classify them as Undifferentiated.

In segment 2–1, at least eight sets of hydrothermal anomalies were detected across four distinct areas (Fig. 4). These include at least four areas of *Low-T* flow, with two (at a minimum) within Area E (#1, #2) and one each in Areas G & H (#7, #8). In Area F, at least four separate sets of ORP anomalies (#3-#7) are observed, all of which coincide with NTU anomalies in the overlying water column. This indicates that at least one source of *High T* venting must be present within Area F together with at least three further sources of hydrothermal flow all of which we can only classify as *Undifferentiated*. No plume surveys were conducted throughout Segment 2-2.

In segment 2–3, evidence for at least one area of hydrothermal activity was observed (Area I, Fig. 5). Here, the coincidence of ORP anomalies close above the seafloor together with NTU anomalies in the overlying water column directly above a volcanic crater can be inferred to reveal the presence of at least one source of *High T* venting. In this instance, black smoker activity has since been verified on the slopes of the crater, using China's *Dragon 2* ROV in 2009 (Tao et al., 2008).

In segment 2–4 (Figs. 6 and 7), 11 sets of NTU and/or ORP anomalies were detected that include at least two *Suspected* sites of venting in Areas J & K (Fig. 6). The remaining \geq 9 sites of seafloor activity revealed by our surveys in this segment include at least 6 separate sources of *High T* venting, with one or more in each of Areas L, M, N and O (Fig. 6) and Areas R and T (Fig. 7). At least two areas of *Low-T* venting are also present, with at least one each Areas Q and S (Fig. 7). In Area P the presence of a near-seabed ORP anomaly underlying NTU anomalies that

may or may not be contiguous with those present at the same depth in Area O preclude us from identifying the nature of its source unambiguously and, hence, it is classified as *Undifferentiated*.

In segment 2–5 (Fig. 8), five distinct sets of ORP anomalies were detected, each indicative of at least one separate source of Low T venting (U, V, W, X & Z). While no evidence of high temperature venting was observed throughout the segment, an area of near-seabed NTU anomalies from close above the seafloor close to the ridge axis can be classified as one final *Suspected* site (Y).

4. Discussion

Using a combination of ORP and optical backscatter data (see preceding section) we have been able to infer that at least 32 discrete sources of submarine venting are present along the EPR between 1.9°N and 4.9°S (Table 1). However, if only NTU anomalies had been used to prospect for hydrothermal activity throughout our study area, only 10 discrete sources of venting (i.e. <33% of the total number of sources inferred) would have been detected. By combining in situ optical backscatter and near-bottom ORP sensors, our analysis of the resultant hydrothermal anomaly data reveals that while as few as 10 inferred hydrothermal sites may result from high-temperature venting, at least 12 of the ≥32 hydrothermal flow sites detected can be attributed to lowtemperature fluid flow. Using these data, we can compare the values for mean site frequency, Fs, that we would calculate from this study when compared to the incidence of vent-distributions that might be predicted for the same spreading rate using the InterRidge vents database (Beaulieu et al., 2015). Note that in the discussion that follows, we include all the surveys conducted along the ridge-axis within our EPR study area (Fig. 1) and not just that subset of our surveys that revealed positive evidence for hydrothermal activity (Figs. 3-9).

Although our survey was not continuous from $1.9^{\circ}N$ to $4.9^{\circ}S$ (for example, we include no survey data for Segment 2-2), what we have assimilated represents 305 km of cumulative track-lines within our study area, including 227 km for which near-bottom ORP sensor data and MAPR data were collected together. It is important to note that some of our surveys included repeat tows over the same section of ridge crest,

S. Chen et al.

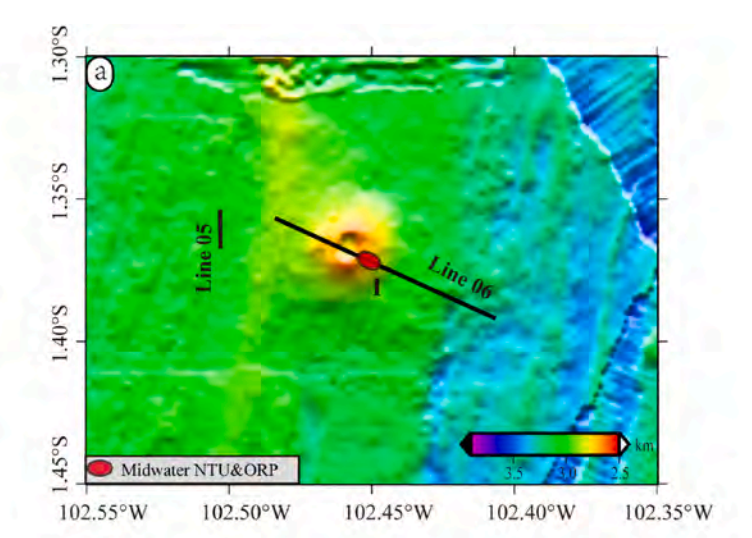
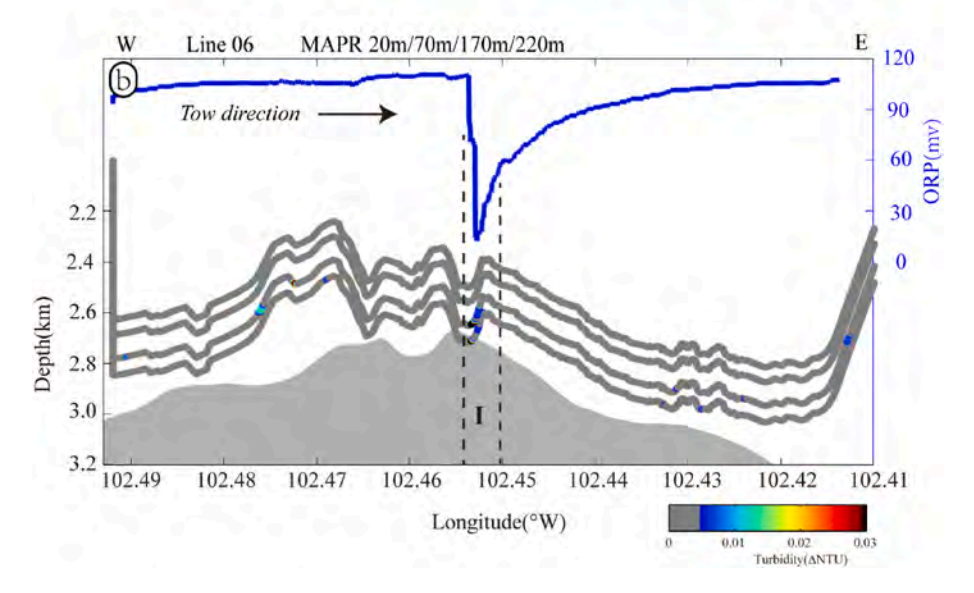


Fig. 5. Hydrothermal anomalies at 1.30–1.45°S EPR (Segment 2–3). (a) Map showing the trajectory of deep-tow survey Lines 05 & 06 with (superimposed) ellipses with the same color coding as for Fig. 3a. (b) Vertical along-axis plot of ORP data and △NTU anomalies from deep-tow survey Line 06. See Fig. 3b for other plot details. Letter I refer to hydrothermal anomaly discussed in the text. (For interpretation of the references to color in this figure legend, the reader is referred to the Web version of this article.)



however (see e.g. Segment 2–5 (Fig. 7)). When we calculate the total *unique* distance surveyed, therefore, (see Chen et al., 2020 for detailed discussion), we have been cautious to base our calculations on the cumulative survey length covered by our surveys. For our MAPR surveys, this reduces to a total of 261 km between 1.9°N and 4.9°S EPR (\sim 34.4% of the total ridge length between these latitudes). 207 km of this survey distance (\sim 27.3% of the total ridge length) was surveyed with co-registered ORP sensors.

Relying solely upon the NTU anomaly data reported here, we would calculate a predicted frequency of venting, Fs, of 4.2 sites per 100 km along the 261 km of ridge-axis where MAPR sensors were deployed. This agrees very closely with Fs of 3.1-3.6 sites per 100 km predicted for spreading rates of 110-132 mm/yr from the InterRidge data-base (Fig. 9). However, when one compares the calculated incidences of venting over just the 207 km of along-axis survey where both ORP and NTU data were collected, a dramatic increase is observed. A minimum of 32 distinct sites of venting occur along this 207 km distance, including all 11 locales with unambiguous evidence of high-temperature venting based on NTU anomalies alone, and results in a much higher incidence of total venting: Fs > 15.5/100 km. This represents a >3-fold increase over what would have been predicted using particle plume anomalies only (Fig. 9), and converges with the 3-6 fold increased abundance in venting reported for intermediate and fast (50-100 mm/yr) spreadingrate ridges by Baker et al. (2016).

These results are important. Over >200 km of survey along the fast spreading (110–132 mm/yr) EPR, 1.9°N-4.9°S, we have shown that a particle-plume only approach to hydrothermal exploration, using optical back-scatter sensors to detect mid-water plumes, can faithfully reproduce the incidence of venting that would have been predicted, using the InterRidge vents data-base (Beaulieu et al., 2015). However, this same study has also shown that such an approach may under-represent the total number of hydrothermally active sources present along the same section of ridge crest by a factor of three or more. These results compare closely with recent work by Baker et al. (2016), which showed that when one allows for low-temperature venting along intermediate and fast spreading ridges, the predicted incidence of venting should be revised upward by a factor of at least 3.

Of course, recognition of the importance of low temperature axial hydrothermal flow is not new from a geophysical perspective. It has long been established that such circulation likely dominates the volume flux of water passing through the ocean crust at ridge axes and that *axial* low-temperature hydrothermal circulation likely represents >50% and perhaps as much as 90% of the heat-flux associated with hydrothermal cooling along the young (0-1 Ma) global ridge axis (see, e.g., Elderfield and Schultz, 1996). More recently, the importance of low-temperature venting as a significant source and/or sink in global-scale ocean biogeochemical cycles has been considered. As part of the international GEOTRACES program, multiple studies in diverse ocean basins have

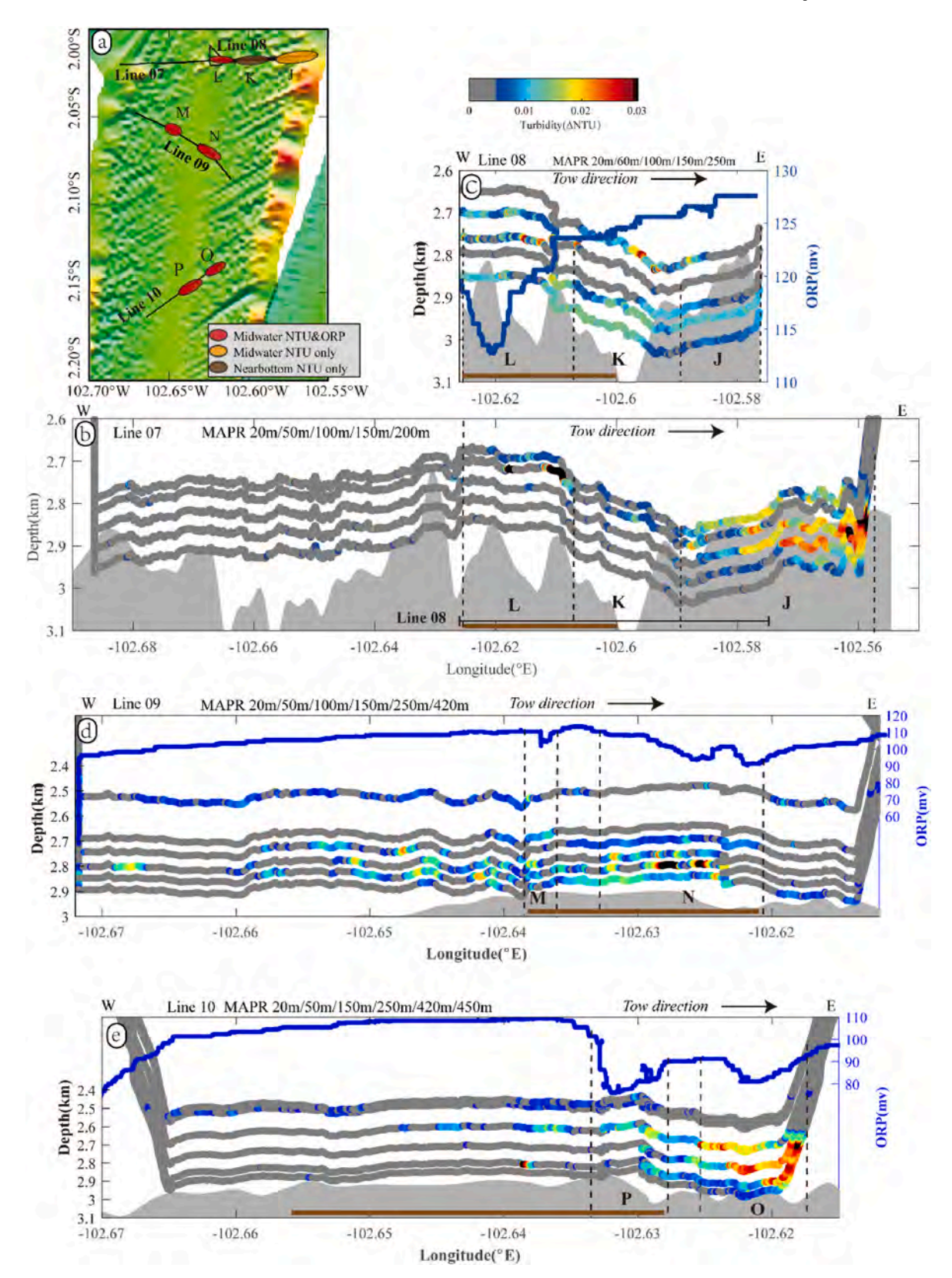


Fig. 6. Hydrothermal anomalies at $2.00-2.20^{\circ}$ S EPR (Segment 2-4, north). (a) Map showing the trajectory of deep-tow survey Lines 07-10 crossing the ridge-axis along this ridge-segment. Superimposed ellipses show the locations of hydrothermal anomalies along each survey line. Color coding as for Fig. 3a but expanded to include: dark brown = near-bottom NTU anomaly only. (b-e) Vertical along-axis plots of ORP data and \triangle NTU from deep-tow survey Lines 08, 07, 09, 10 respectively. See Fig. 3b for other plot details. Letters J-P refer to hydrothermal anomalies discussed in the text. (For interpretation of the references to color in this figure legend, the reader is referred to the Web version of this article.)

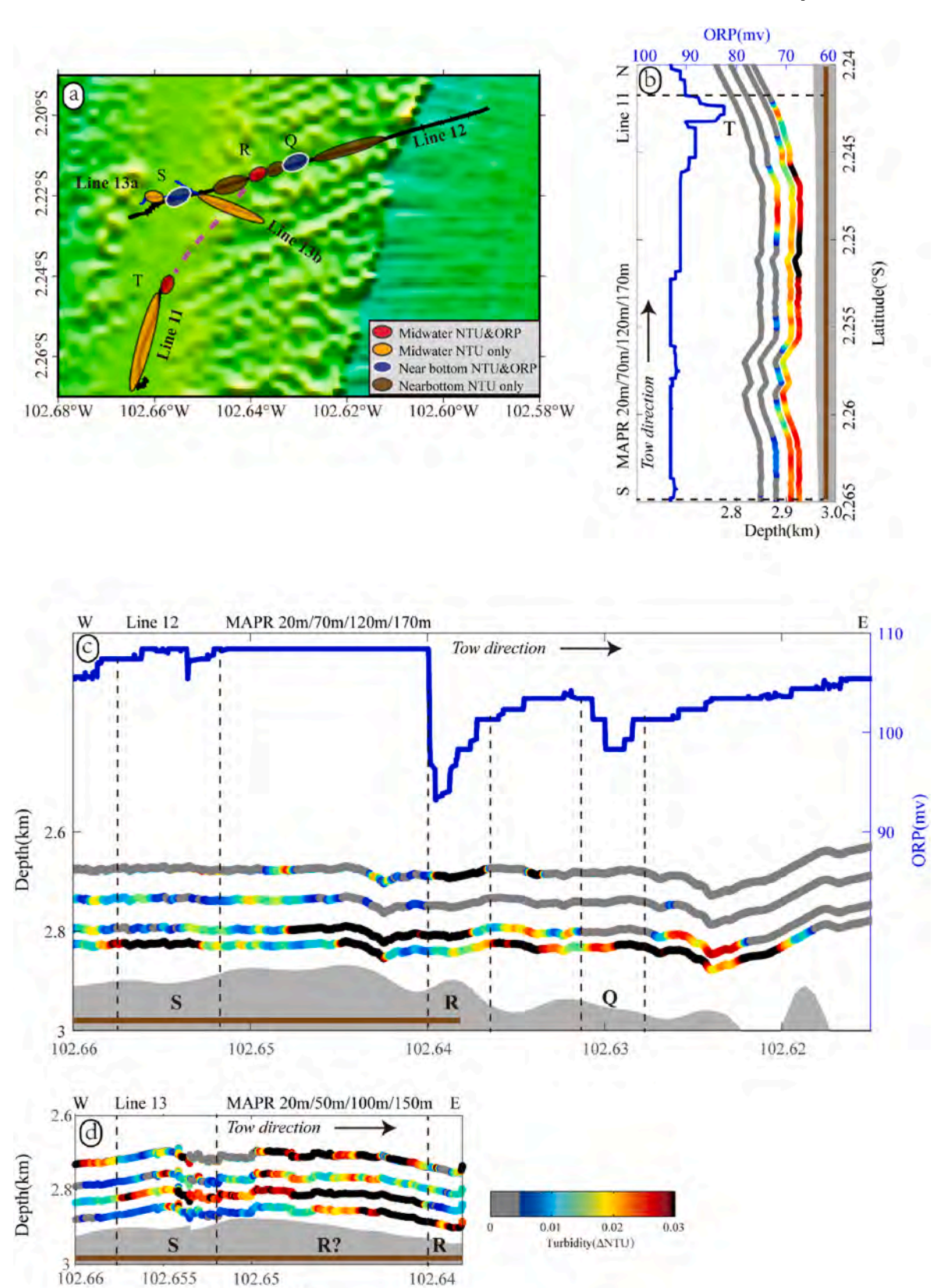


Fig. 7. Hydrothermal anomalies at $2.20-2.30^{\circ}$ S EPR (Segment 2–4, south). (a) Map showing the trajectory of deep-tow survey Lines 11-13 crossing the ridge-axis along this ridge-segment. Superimposed ellipses show the locations of hydrothermal anomalies along each survey line (color coding as for Fig. 6a). (b–d) Vertical along-axis plots of ORP data and \triangle NTU anomalies from deep-tow survey Lines 11, 12, 13 respectively. See Fig. 3b for other plot details. Letters Q-T refer to hydrothermal anomalies discussed in the text. (For interpretation of the references to color in this figure legend, the reader is referred to the Web version of this article.)

Longitude(°W)

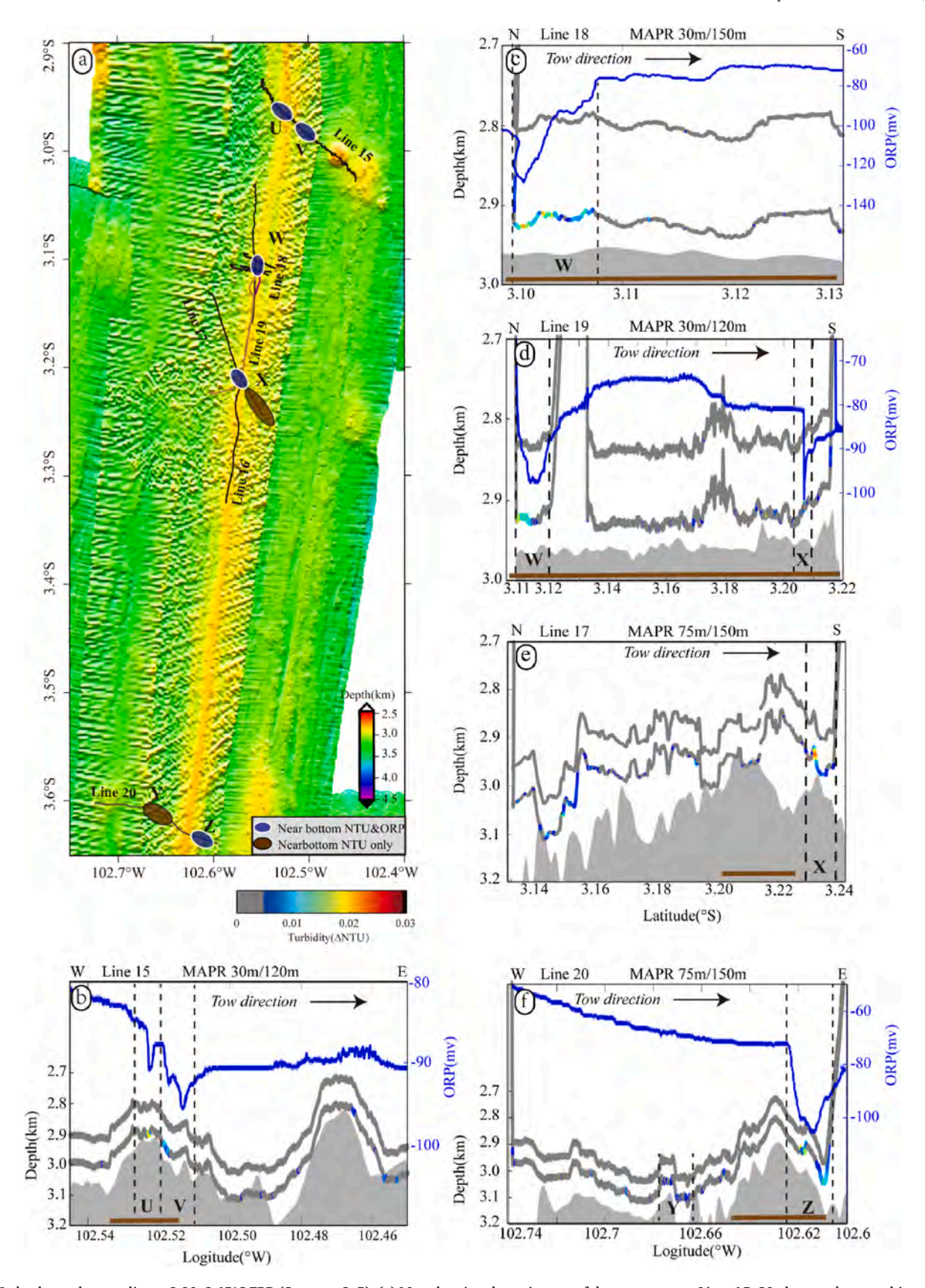


Fig. 8. Hydrothermal anomalies at 2.90–3.65°S EPR (Segment 2–5). (a) Map showing the trajectory of deep-tow survey Lines 15–20 along and across this segment of the ridge-axis. Superimposed ellipses show the locations of hydrothermal anomalies along each survey line (color coding as for Fig. 6a). (b–f) Vertical along-axis plots of ORP data and △NTU anomalies from deep-tow survey Lines 15, 18, 19, 17 and 20, respectively. See Fig. 3b for other plot details. Letters U-Z refer to hydrothermal anomalies discussed in the text. (For interpretation of the references to color in this figure legend, the reader is referred to the Web version of this article.)

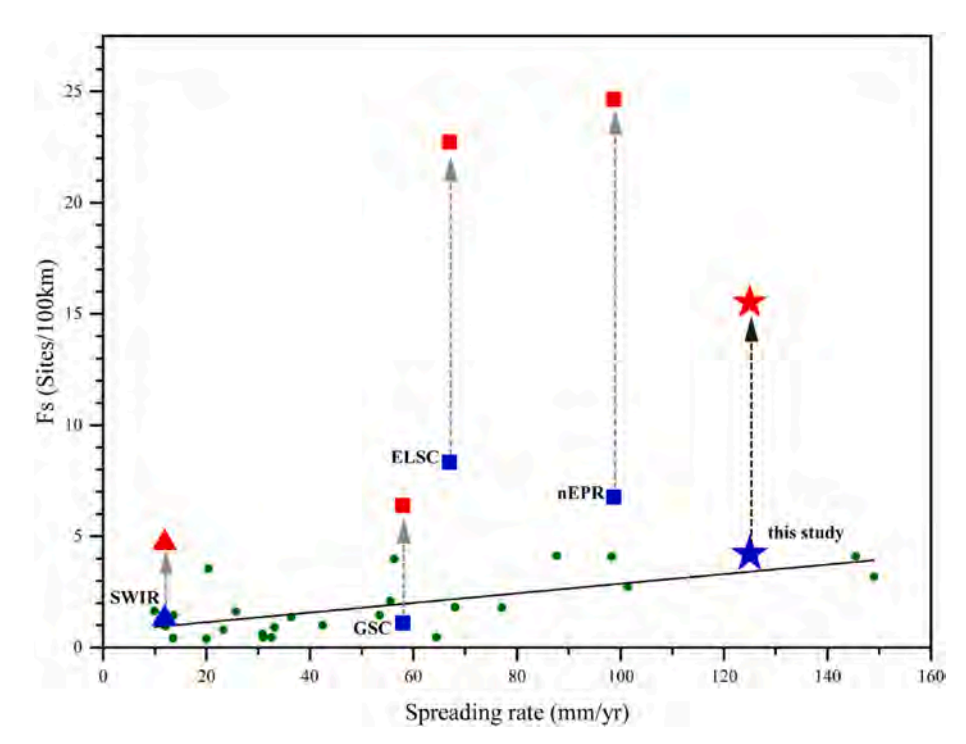


Fig. 9. Plot showing frequency of occurrence of hydrothermal vent fields along axis (Fs) vs. full ridge spreading rate (mm/yr) for 27 ridge sections represented in the InterRidge Vents database (green circles). Blue and red stars represent a synthesis of the results from this study; blue and red squares show equivalent values of (Fs) for the three sections of medium-fast spreading mid-ocean ridge discussed by Baker et al. (2016); blue and red triangles show the equivalent values for Segment 27, SW Indian Ridge (Yue et al., 2019). Blue symbols represent the incidence of high-temperature venting along axis (Fs) that would be predicted using NTU anomalies only from each of those studies. Red symbols represent the increased incidences of venting resulting from the addition of in situ ORP sensor data along those same ridge-sections. (For interpretation of the references to color in this figure legend, the reader is referred to the Web version of this article.)

Table 1
Distributions and types of hydrothermal anomaly detected EDR 1.0°N.4.0°S

Seg	Area	Start Lat	Start Lon	End Lat	End Lon	Extent (km)	Plume Depth(m)	Max ΔNTU value	ORP (mV)	Flag* ¹	sites* ² (Total)	Sites (Hi-T)	Sites (Lo- T)	Sites (Undiff-)	Sites (Suspected)
S1	A	1.88	-102.29	1.79	-102.30	10.15	2770-2900	0.012	no	I	≥1	≥1	0	0	0
	В	1.76	-102.30	1.66	-102.29	11.05	2770-2820	0.015	-160	III	≥5	≥ 1	\geq 0	4	0
	C	1.66	-102.29	1.65	-102.28	1.59	2820	No	-100	II	≥ 1	0	≥ 1	0	0
	D	1.65	-102.28	1.59	-102.28	5.74	2760-2850	0.007	-70	III	\geq 2	≥ 1	\geq 0	1	0
S2-	E	1.07	-102.18	1.04	-102.18	2.79	2650-2700	No	-90	II	\geq 2	0	\geq 2	0	0
1	F	1.04	-102.18	1.00	-102.19	5.49	2750-2900	0.03	-30	III	≥4	≥ 1	\geq 0	3	0
	G	1.00	-102.19	0.97	-102.20	2.61	2700	0.02	-5	II	1	0	1	0	0
	H	0.97	-102.20	0.91	-102.20	6.67	2700	0.008	-8	II	1	0	1	0	0
S2- 3	I	-1.37	-102.45	-1.37	-102.45	0.30	2750	0.04	-100	I	1	1	0	0	0
52-	J	-2.01	-102.56	-2.02	-102.59	3.44	2750-2970	0.03	no	V	\geq 0	\geq 0	0	0	1
4	K	-2.02	-102.59	-2.02	-102.61	2.14	2950	0.012	no	V	\geq 0	\geq 0	≥0	0	1
	L	-2.02	-102.61	-2.02	-102.63	2.18	2750	0.065	-8	I	1	1	0	0	0
	M	-2.06	-102.64	-2.07	-102.64	0.25	2700	0.02	-10	I	1	1	0	0	0
	N	-2.07	-102.63	-2.08	-102.62	1.54	2700-2900	0.06	-20	I	≥ 1	≥ 1	0	0	0
	O	-2.14	-102.62	-2.13	-102.62	0.66	2600-3000	0.03	-15	I	1	1	0	0	0
	P	-2.14	-102.63	-2.15	-102.63	1.14	2600-2950	0.015	-30	IV	≥ 1	\geq 0	0	1	0
	Q	-2.21	-102.63	-2.21	-102.63	0.58	2800-2820	0.04	-7	II	≥ 1	0	≥ 1	0	0
	R	-2.21	-102.64	-2.22	-102.64	0.50	2700-2820	0.062	-18	I	≥ 1	≥ 1	0	0	0
	S	-2.22	-102.65	-2.22	-102.66	0.48	2750-2820	0.055	-5	II	1	0	1	0	0
	T	-2.24	-102.66	-2.26	-102.66	2.50	2870-2950	0.03	-10	I	1	1	0	0	0
S2-	U	-2.97	-102.52	-2.98	-102.52	0.36	2870-2920	No	-5	II	1	0	1	0	0
5	V	-2.98	-102.52	-2.99	-102.51	1.98	2900-3000	No	-10	II	≥ 1	0	≥ 1	0	0
	W	-3.10	-102.55	-3.12	-102.56	2.44	2900-2930	0.02	-60	II	≥ 1	0	≥ 1	0	0
	X	-3.21	-102.57	-3.24	-102.55	4.21	2900-2950	No	-20	II	≥ 1	0	≥ 1	0	0
	Y	-3.61	-102.68	-3.61	-102.67	1.25	3030-3100	0.012	no	V	\geq 0	0	\geq 0	0	1
	Z	-3.64	-102.63	-3.64	-102.61	2.04	2900-3050	0.02	-35	II	≥ 1	0	≥ 1	0	0
								Total			≥32	≥11	≥12	9	≥3

^{*}¹ Flag: an indication of which plumes were used to calculate Fs by each method. I represent High-T plume only. II represent Low-T plume only. III represent High-T plume with undifferentiated hydrothermal site. IV represent Undifferentiated hydrothermal sits. V represent Suspected, or an identified area is considered an extension of another area, so not included as a separate site.

shown that a small proportion of the total Fe released on-axis by hydrothermal venting can persist over long distances into the interior of ocean basins (German et al. Phil Trans Roy Soc, 2016). Independently,

modelling conducted by SCOR Working Group 135 has predicted that such long-range and persistent Fe supply might derive predominantly from low-temperature hydrothermal flow (German et al., 2015). Similar

^{*&}lt;sup>2</sup> To ensure that our calculations remain conservative we do not include any suspected sites (near-seabed NTU anomalies without accompanying ORP anomalies) in calculating the total number of hydrothermal sites.

to the study of Baker et al. (2016), our near-seafloor ORP sensor data reveal that there is an abundance of low-temperature venting along fast-spreading and intermediate-spreading ridge axes that is out of redox equilibrium, hence, *geochemical* equilibrium with the overlying water column. Could fluid flow of this form be responsible for the large fluxes of Fe that have been shown to escape from submarine venting and which, in the limit, may stimulate surface ocean productivity via upwelling into high nutrient low chlorophyll regions of the surface ocean (Resing et al., 2015; Jenkins, 2020)? That hypothesis has gained fresh impetus within the international GEOTRACES program, recently, and is only fuelled by seafloor discoveries of the type presented here. Clearly, chemically anomalous Low T fluid flow sites are present in abundance along fast spreading mid ocean ridges. A key priority for future research will be to investigate what the biogeochemical fluxes associated with such Low T venting might be.

5. Summary and conclusions

Observations using a combination of near-bottom ORP sensing together with water-column particle plume surveys to explore for seafloor hydrothermal activity have been conducted along ~758 km of second-order ridge segments of the fast-spreading (110-132 mm/yr) East Pacific Rise (EPR) between 1.9°N and 4.9°S. Our surveys predict an incidence of 4.2 high-temperature vent sites per 100 km of ridge axis when only above-bottom particle plumes are considered, in close agreement with what would have been predicted from the global InterRidge vents database. However, if we include the use of nearbottom ORP sensor analyses in our surveys, the total number of hydrothermal sources detected within our study area increases dramatically from ≥10 sites to at least 32 distinct sources of submarine venting an increase of at least 3-fold in the frequency of active discharge sites. Low-temperature emissions are difficult to detect using particle-plume only surveys, but because these fluids are also out of geochemical (redox) equilibrium with the surrounding deep ocean water column, they are easily detected with ORP sensors. Consequently, our findings demonstrate the importance of the role of low-temperature hydrothermal fluxes in global-scale ocean biogeochemical cycles.

Declaration of competing interest

The authors declare that they have no known competing financial interests or personal relationships that could have appeared to influence the work reported in this paper.

Acknowledgements

We acknowledge the science parties and crew of Dayang YiHao expedition DY17 in 2005, DY20 in 2008, DY21 in 2009 and DY22 in 2011 for data collection. Fieldwork for this study was funded by National Key Research and Development Program of China (2018YFC0309901), China Ocean Mineral Resources R & D Association (COMRA) Project (DY135-S1-1-01,02,09) and Natural Science Foundation of Zhejiang Province (LQ19D060008). SC recognizes financial support from China Scholarship Council which supported her visit to WHOI where the data analysis for this paper occurred (201808330070); CG recognizes financial support from US National Science Foundation grant OCE-1755571 and from WHOI. We are grateful to the contributions made by Guanghai Wu, Yongshun John Chen, Jianyu Ni, Jian Lin, Xin Su, Jianping Zhou and Yuan Wang - both for overseeing the cruises during which the ORP and MAPR sensor data reported here were collected but also for their thoughtful suggestions during those cruises. All the data used to generate the figures now can be obtained from the

accompanying Data Brief (Chen et al., 2020).

References

- Baker, E.T., German, C.R., 2004. On the global distribution of hydrothermal vent fields. In: German, C.R., Lin, J., Parson, L.M. (Eds.), Mid-ocean Ridges: Hydrothermal Interactions between the Lithosphere and Oceans, vol. 148, pp. 245–266.
- Baker, E.T., Milburn, H.B., 1997. MAPR: a new instrument for hydrothermal plume mapping. RIDGE Events 8 (1), 23–25.
- Baker, E.T., Hémond, C., Briais, A., Maia, M., Scheirer, D.S., Walker, S.L., Chen, Y.J., 2014. Correlated patterns in hydrothermal plume distribution and apparent magmatic budget along 2500 km of the Southeast Indian Ridge. G-cubed 15 (8), 3198–3211. https://doi.org/10.1002/2014gc005344.
- Baker, E.T., Resing, J.A., Haymon, R.M., Tunnicliffe, V., Lavelle, J.W., Martinez, F., Ferrini, V., Walker, S.L., Nakamura, K., 2016. How many vent fields? New estimates of vent field populations on ocean ridges from precise mapping of hydrothermal discharge locations. Earth Planet Sci. Lett. 449, 186–196. https://doi.org/10.1016/j. epsl.2016.05.031.
- Beaulieu, S.E., Baker, E.T., German, C.R., 2015. Where are the undiscovered hydrothermal vents on oceanic spreading ridges? Deep Sea Research II 121, 202–212. https://doi.org/10.1016/j.dsr2.2015.05.001i.
- Beaulieu, S.E., Baker, E.T., German, C.R., Maffei, A., 2013. An authoritative global database for active submarine hydrothermal vent fields. G-cubed 14 (11), 4892–4905. https://doi.org/10.1002/2013gc004998.
- Chen S., Tao C., German C. R., 2020, Hydrothermal plume detection dataset from Chinese cruises to the equatorial East Pacific Rise. Data In Brief.
- Corliss, J.B., Dymond, J., Gordon, L.I., Edmond, J.M., Herzen, R.P.v., Ballard, R.D., Green, K., Williams, D., Bainbridge, A., Crane, K., Andel, T.H.V., 1979. Submarine thermal springs on the galápagos rift. Science 203 (4385), 1073–1083.
- DeMets, C., Gordon, R.G., Argus, D.F., Stein, S., 1990. Current plate motions. Geophys. J. Int. 101, 425–478. https://doi.org/10.1111/j.1365-246X.1990.tb06579.x.
- Elderfield, H., Schultz, A., 1996. Mid-Ocean ridge hydrothermal fluxes and the chemical composition of the ocean. Annual Review of Earth & Planetary ences 24 (1), 191–224.
- German, C.R., Casciotti, K.A., Dutay, J.C., et al., 2016. Hydrothermal impacts on trace element and isotope ocean biogeochemistry. Philosophical transactions. Series A, Mathematical, physical, and engineering ences 2081, 374.
- German, C.R., Legendre, L.L., Sander, S.G., Niquil, N., Luther, G.W., Bharati, L., Han, X., Le Bris, N., 2015. Hydrothermal Fe cycling and deep ocean organic carbon scavenging: model-based evidence for significant POC supply to seafloor sediments. Earth Planet Sci. Lett. 419, 143–153. https://doi.org/10.1016/j.epsl.2015.03.012.
- German, C.R., Yoerger, D.R., Jakuba, M., Shank, T.M., Langmuir, C.H., Nakamura, K.-i., 2008. Hydrothermal exploration with the autonomous benthic explorer. Deep Sea Res., Part I 55, 203–219.
- Jenkins, W.J., 2020. Using excess 3he to estimate southern ocean upwelling time scales. Geophys. Res. Lett. 47.
- Klinkhammer, G., Rona, P., Greaves, M., Elderfield, H., 1985. Hydrothermal manganese plumes in the Mid-Atlantic Ridge rift valley. Nature 314, 727–731.
- Klinkhammer, G., Elderfield, H., Greaves, M., Rona, P., Nelsen, T., 1986. Manganese geochemistry near high-temperature vents in the Mid-Atlantic Ridge rift valley. Earth Planet Sci. Lett. 80, 230–240.
- $\label{loss} Lonsdale, P., 1989. Segmentation of the pacific-nazca spreading center, $1^\circ N-20^\circ S.$ J. Geophys. Res. 94 (B9), $12197.$ https://doi.org/10.1029/JB094iB09p12197.$
- Nelsen, T.A., Klinkhammer, G.P., Trefry, J.H., Trocine, R.P., 1987. Real-time observation of dispersed hydrothermal plumes using nephelometry: examples from the Mid-Atlantic Ridge. Earth Planet Sci. Lett. 81 (2), 245–252.
- Resing, J.A., Sedwick, P.N., German, C.R., Jenkins, W.J., Moffett, J.W., Sohst, B.M., Tagliabue, A., 2015. Basin-scale transport of hydrothermal dissolved metals across the South Pacific Ocean. Nature 523 (7559), 200–203. https://doi.org/10.1038/ nature14577.
- Shank, T.M., Fornari, D.J., Wigham, B., Scheirer, D., Getsiv, J., Perfit, M., Tolstoy, M., 2000. Biology of Newly-Discovered "AHA" Hydrothermal Vent Fields Near 144 N on the East Pacific Rise Axis. EOS Trans. AGU, p. F1076.
- Spiess, F.N., Macdonald, K.C., Atwater, T., Ballard, R., Carranza, A., Cordoba, D., Cox, C., Garcia, V.M.D., Francheteau, J., Guerrero, J., Hawkins, J., Haymon, R., Hessler, R., Juteau, T., Kastner, M., Larson, R., Luyendyk, B., Macdougall, J.D., Miller, S., Normark, W., Orcutt, J., Rangin, C., 1980. East Pacific Rise: hot springs and geophysical experiments. Science 207 (4438), 1421–1422.
- Tao, C., Lin, J., Wu, G., German, C.R., et al., 2008. First Active Hydrothermal Vent Fields Discovered at the Equatorial Southern East Pacific Rise. AGU Fall Meeting Abstract, pp. V41B–V2081.
- Walker, S.L., Baker, E.T., Massoth, G.J., Hey, R.N., 2004. Short-term variations in the distribution of hydrothermal plumes along a superfast spreading center, East Pacific Rise, 27°30′–32°20′S. G-cubed 5 (Q12005), 1–9.
- Yue, X., Li, H., Ren, J., Tao, C., Zhou, J., Wang, Y., Lu, X., 2019. Seafloor hydrothermal activity along mid-ocean ridge with strong melt supply: study from segment 27, southwest Indian ridge. Sci. Rep. 9 (1), 9874. https://doi.org/10.1038/s41598-019-46299-1